Higher-order topological phase diagram revealed by anomalous Nernst effect in a Janus ScClI monolayer

Ning-Jing Yang and Jian-Min Zhang [*]

Fujian Provincial Key Laboratory of Quantum Manipulation and New Energy Materials, College of Physics and Energy, Fujian Normal University, Fuzhou 350117, China
and Fujian Provincial Collaborative Innovation Center for Advanced High-Field Superconducting Materials and Engineering, Fuzhou 350117, China

Higher-order topological properties of two-dimensional (2D) magnetic materials have recently been proposed. In 2D ferromagnetic Janus materials, we find that ScClI is a second-order topological insulator. Using the tight-binding approximation, we develop a multiorbital model that adequately describes the high-order topological states of ScClI. Further, we give the complete high-order topological phase diagram of ScClI, based on the external field modulation of the magnetovalley coupling and energy levels. The 2D ScClI has a pronounced valley polarization. This type of magnetovalleytronics results in different insulating phases to exhibit completely different anomalous Nernst conductance. Through valleytronics, we establish a link between the topological insulator and the valley Nernst effect, thus constructing an anomalous valley Nernst conductance map that corresponds to the topological phase diagram. We utilize the characteristics of valley electronics to link higher-order topological materials with the anomalous Nernst effect, which has potential implications for high-order topological insulators and valley electronics.

I. INTRODUCTION

Recently, two-dimensional (2D) high-order topological insulators (HOTIs) have received great attention [1–6]. Prior to this, higher-order topological states in three-dimensional Bi, $MnBi_{2n}Te_{3n+1}$, and $EuIn_2As_2$ have received attention [7–11]. However, higher-order topological corner states hidden in the 2D transition metal $2H$-MoS_2 family have only recently been discovered [1–3]. They are all protected by space inversion symmetry and have a nonzero topological corner charge [12–14]. The analogous higher-order topological properties can also be extended to 2D ferromagnetic and ferroelectric materials [15,16]. However, there is still a need for a more detailed and comprehensive analysis of high-order topological multiorbital systems and phase transition processes, as well as a stronger connection to valleytronics. Moreover, compared to photonic and phononic crystals, which are highly manipulated [17,18], there are still relatively few electronic materials with higher-order topologies. Therefore, finding new 2D HOTI materials is important and significant.

Two-dimensional materials with a honeycomb structure have strong energy valley properties [19–21]. For 2D ferromagnetic materials, the intrinsic ferromagnetic order couples with the energy valleys to produce giant valley polarization [4,22] and leads to large differences in the Berry curvature of the K/K' valleys. Since the Berry curvature is analogous to an equivalent magnetic field [23], the anomalous velocity transmitted to the electrons leads to valley currents [21–24]. Applications on this basis consist of the valley Hall effect

[24] and the anomalous Nernst effect [22]. In particular, the anomalous Nernst effect has been widely measured and applied experimentally [25–31]. The anomalous Nernst effect on $2H$-MoS_2 family materials was discussed earlier by Yu *et al.* [31]. It can be predicted that there is a certain connection between the topological properties and the valley Nernst effect. Such a connection has been rarely mentioned. Consequently, associating topological phase transitions with the anomalous valley Hall effect holds significant physical significance.

In this paper, we discover that monolayer ScClI is a second-order topological insulator (SOTI), exhibiting second-order topological corner states in a 2D triangular quantum dot. Using the multiorbital tight-binding approximation theory, we learn that the p orbitals of the halogen elements are indispensable for higher-order topology. It is not possible to show this by only considering the d orbitals. Next, by applying an external field to change the magnetovalley coupling strength and energy level difference, we provide the complete topological phase diagram of 2D Janus ScClI. ScClI mainly undergoes the topological phase transition process of SOTIs, quantum anomalous valley Hall insulators (QAVHIs), and normal insulators (NIs). Due to the strong valley electronic properties of ScClI, the phenomena of SOTIs, QAVHIs, and NIs exhibit distinct characteristics in the thermally induced anomalous Nernst effect. Based on this foundation, we provide anomalous Nernst conductance maps that correspond to the higher-order topological phase diagram. Our results effectively link high-order topology with the anomalous Nernst effect of thermal excitation, which is of great significance for the measurement and application of experimental electronic devices.

*Corresponding author: jmzhang@fjnu.edu.cn
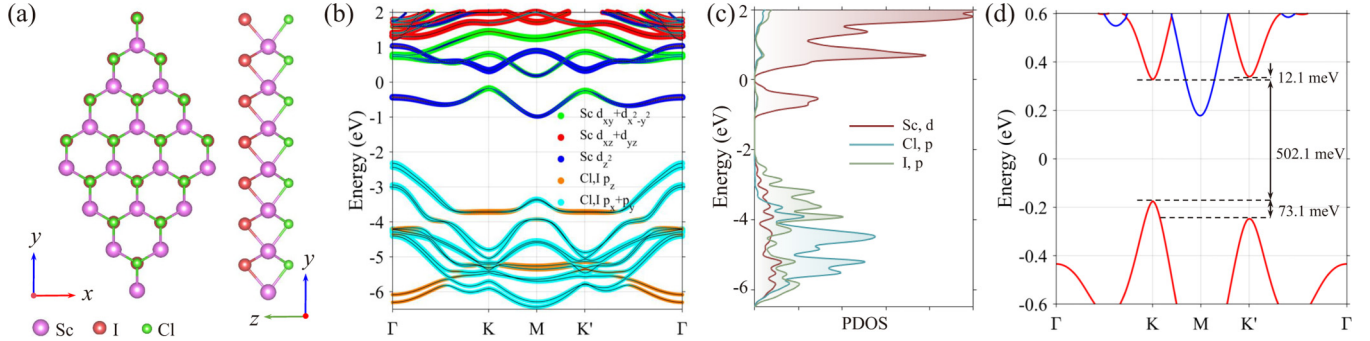
FIG. 1. (a) Top and side views of ScClI. (b) In the out-of-plane ferromagnetic state, a fat band of projected orbitals is present. (c) The projected density of states (PDOS) of the system. (d) Spin-polarized energy bands near the Fermi level. Red and blue lines indicate spin-up and spin-down states.

II. METHODS

First-principles calculations based on density functional theory (DFT) are conducted using the Vienna *ab initio* simulation package (VASP) [32,33]. The electronic exchange-correlation interactions are treated using the Perdew-Burke-Ernzerhof (PBE) generalized gradient approximation (GGA) [34,35]. For two-dimensional materials, a minimum of 15 Å vacuum layer is included. The energy cutoff for the plane-wave basis is set to 500 eV, and a $10 \times 10 \times 1$ k mesh is employed for Brillouin-zone sampling. The convergence threshold for the maximum force during structural optimization is set to be less than 0.01 eV/Å, and the energy convergence criterion is set to be 10^{-6} eV. We apply the GGA + U method to correct the Coulomb repulsion interactions of the Sc atom's d orbitals, with a typical value of $U = 3$ eV [36,37]. The parity of the occupied states is calculated using the IRREP program [38]. Additionally, a tight-binding model based on maximally localized Wannier functions (ML-WFs) is constructed using the WANNIER90 and WANNIERTOOLS packages [39,40].

III. RESULTS AND DISCUSSION

The crystal structure of the two-dimensional Janus honeycomb material ScClI is shown in Fig. 1(a). Its fat band reveals a predominant contribution from the d orbitals of Sc in the vicinity of the Fermi energy level. From PDOS, it can be seen that the low-energy states dominated by p orbitals also contain contributions of d orbitals from Sc, as shown in Fig. 1(c). In the out-of-plane ferromagnetic state, magnetovalley coupling induces polarization at K and K', as illustrated in Fig. 1(d). The measured energy level difference between valence electrons in the K and K' valleys is 73.1 meV, and the band gap in the spin-up energy band of the K valley is determined to be 502.1 meV. Although the system is an indirect band-gap insulator in its fully relaxed state, it can be transformed into a direct band-gap insulator by applying strain.

To verify the high-order topological properties of ScClI, we first calculate the higher-order topological indices $Q_c^{(3)}$ of the system, which is protected by the symmetry of the C_3 rotation symmetry. For the rotation eigenvalue calculation of all occupied states on the high-symmetry points in the Brillouin zone, one can take $[K_n^{(3)}] = \#K_n^{(3)} - \#\Gamma_n^{(3)}$, where # denotes

the counting about the symmetry eigenvalues at the points K and Γ. The eigenvalues of the C_3 rotations are defined as $e^{2\pi i(n-1)/3}$ (for $n = 1, 2, 3$). The topological indices [12,13] of the HOTI are

$$\chi^{(3)} = \left(\left[K_1^{(3)} \right], \left[K_2^{(3)} \right] \right), \quad Q_c^{(3)} = \frac{e}{3} \left[K_2^{(3)} \right] \bmod e, \quad (1)$$

where e is the charge of the free electron. The upper indicator (3) represents C_3 symmetry. By performing DFT calculations, we obtain the wave functions of all occupied Bloch states below the Fermi level. Afterwards, utilizing the IRREP program [38], we calculate the symmetry eigenvalues of these wave functions upon application of the C_3 rotation operator. With them, the topological indicator $\chi^{(3)} = (1, 2)$ and the nonzero corner charge $Q_c^{(3)} = 2e/3$ are obtained. So, we can conclude that the in-gap corner states of the system are topologically protected.

For this system, the magnetovalley coupling gives rise to a giant valley polarization. This depends on the magnitude of the magnetic moment outside the surface, and the valley polarization disappears when a magnetic moment inside the surface is applied. This is illustrated in Figs. S4(a)– S4(c) of the Supplemental Material [41]. Then, to comprehensively capture the essential physical characteristics of higher-order topology, we develop a simplified multiorbital tight-binding (TB) model based on the Wannier functions. To provide a complete representation of HOTI, the TB model incorporates the entire set of five d orbitals and six p orbitals (from Sc, Cl, and I, respectively), with a focus on the nearest-neighbor orbital hopping. From Wannier fitting, the system shows both spin-orbit coupling (SOC) and valley polarization due to intrinsic magnetism. Thus, the Hamiltonian can be written as

$$H = \sum_{\langle i,j \rangle \alpha, \beta} \left(t_{ij}^{\alpha, \beta} c_{i\alpha}^{\dagger} c_{j\beta} + \text{H.c.} \right) + t_{\text{soc}} \mathbf{L} \cdot \mathbf{S} + m_z \mathbf{M} \cdot \mathbf{S}, \quad (2)$$

where $c_{i\alpha}^{\dagger}$ ($c_{j\beta}$) represents the electron creation (annihilation) operator for the orbital α (β) located at position i (j). t_{soc} denotes the strength of the SOC, and $M = (M_x, M_y, M_z)$ represents the magnetic moment direction with m_z intensity. S is the Pauli matrix.

Under this TB model, we have successfully identified higher-order topological corner states in the fully relaxed structure of ScClI. The electronic band structure of the
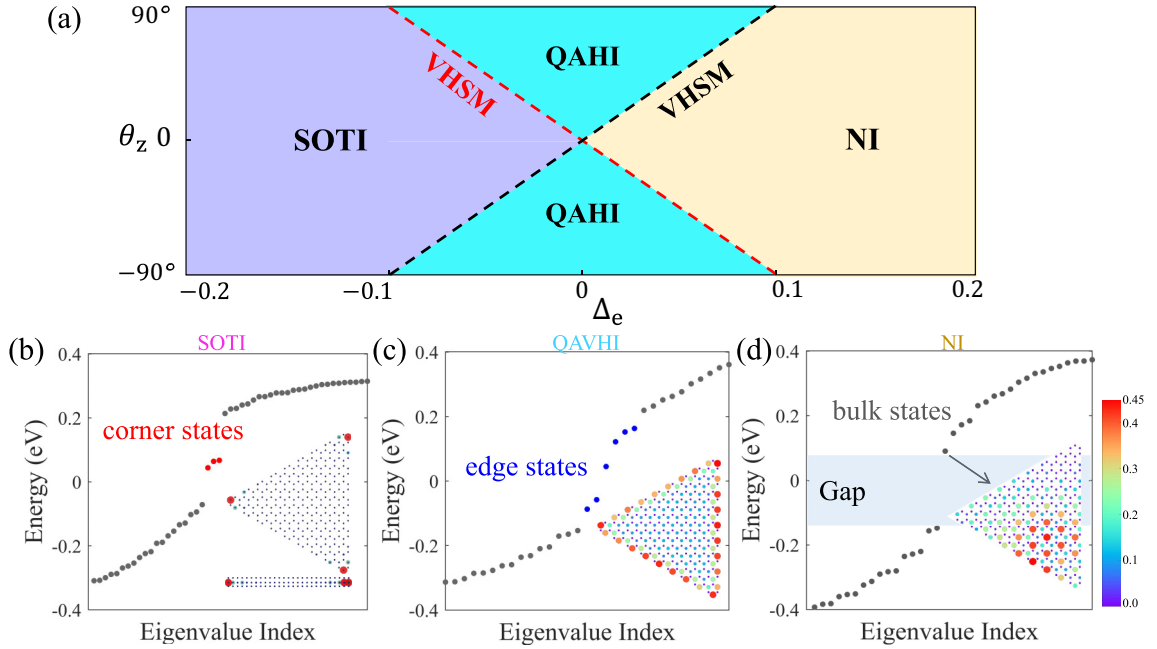
FIG. 2. (a) The complete phase diagram as a function of the magnetic moment direction θ_z and the energy level difference Δ_e. (b) Energy spectrum of triangular armchair nanosheets, and the total wave-function distribution in real space for the corner states within the band gap of the energy spectrum. (c) The quantum dot energy spectrum of QAVHI is displayed, with blue dots marking the boundary states near the Fermi energy. The inset shows the wave-function distribution. (d) The energy spectrum of NI, illustrating the wave-function distribution of bulk states.

triangular quantum dot is depicted in Fig. 2(b), where the presence of the red color in the middle of the band gap represents the corner states. The wave functions of the corner states are localized on the corners of the quantum dots. Higher-order topological corner states are the result after a full consideration of the p, d orbitals. Conversely, if we focus solely on the d-orbital contribution from the Sc atom, the presence of only one occupied band below the Fermi level results in the corner charge $Q_c^{(3)} = 0$. In this way, we will not obtain in-gap corner states that are topologically protected, as shown in Fig. S2. Moreover, from the PDOS, it can be seen that there is a certain coupling between the d and p orbitals. So, establishing a TB model for multiple orbits is effective.

Next, we can achieve higher-order topological phase transitions by tuning the angle θ_z of the magnetic moment and the energy level difference Δ_e between the d_{xy} and d_{z^2} orbitals at the K-valley vertex. The angle θ_z primarily influences the magnitude of valley polarization, while Δ_e induces band inversions, leading to a transition from a SOTI to a QAVHI. Due to the magnetovalley coupling, after the first band inversion, the system becomes a QAVHI with Chern number $C = 1$. Following the second band inversion, the system transforms into a trivial insulator. Notably, at the critical point of the topological phase transition, the system manifests a valley-Hall semimetal phase at the K valley during the initial inversion and at the K' valley during the subsequent inversion. Figure 2(a) displays the complete phase diagram, showing the progression SOTI-VHSM-QAVHI-VHSM-NI.

For the above topological phase transition process, we can realize it by applying tensile strain. After experiencing the first energy band inversion in the K valley, the system

becomes QAVHI. At this time, the energy spectrum of the triangular quantum dots undergoes a transformation, wherein the band gap disappears and is supplanted by a continuum of edge states, as shown in Fig. 2(c). With increasing strain, the second energy band inversion occurs in the K' valley. The system behaves as a normal insulator. The corresponding energy spectrum exhibits a band gap with no corner states or edge states within it. Additionally, both sides of the band gap show localized features within the body, as shown in Fig. 2(d). At tensile strain magnitudes of 2.05% and 2.34%, the system reaches the phase boundary, transitioning into a valley-half semimetal, as shown in Fig. 3(a). In both strain ranges, the Chern number of the system is 1, and Fig. 3(b) illustrates the Wannier charge center (WCC) of the system. The surface states and quantum anomalous Hall conductance platform of QAVHI are shown in Figs. 3(c) and 3(d), respectively.

The giant valley polarization property, due to the intrinsic magnetism of the system, has attracted our attention because it will bring about a difference in the Berry curvature at the valley of K/K'. Berry curvature is the same as adding an equivalent magnetic field to the system, which causes the electrons to acquire anomalous velocities [23]. We can exploit this property to obtain tunable valley flows.

Since the Berry curvature-induced valley flow depends on the neighborhood of the Fermi energy level and is related to the valley degree of freedom, we can use the two-band $k \cdot p$ model to characterize the physical properties of valley locking. The Hamiltonian of the two-band model can be written as

$$\mathcal{H} = at(k_x\sigma_x + \eta k_y\sigma_y) + \frac{\Delta_e}{2}\sigma_z + \sin\theta_z\eta m_z\sigma_z, \quad (3)$$
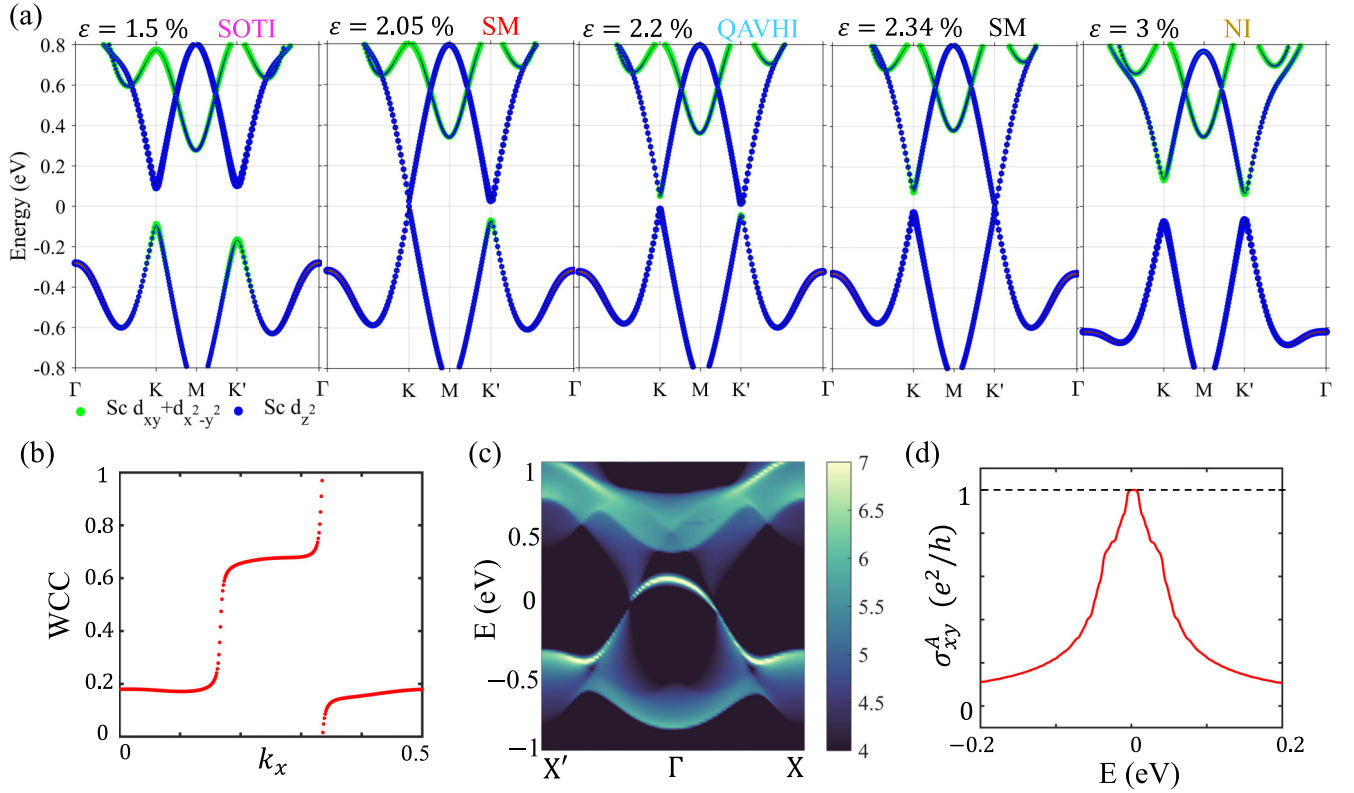
FIG. 3. (a) Projected energy band evolution in the 1.5%–3% strain range. WCC and surface band of QAVHI at 2.2% strain are shown in (b) and (c), respectively. (d) Plot of quantum anomalous Hall conductance vs energy.

where is η the valley index, a is the lattice constant, and t is the hopping integral. m_z denotes the strength of the magnetovalley coupling. $\sigma_{x,y,z}$ is the Pauli matrix. The absence of a spin indicator is attributed to the spin polarization in the vicinity of the Fermi energy level. The effective mass $\Delta_m = \Delta_e/2 + \sin\theta_z\eta m_z$. The energy eigenvalues are

$$E_\eta^n = n\sqrt{(kat)^2 + \Delta_m^2},\qquad(4)$$

where $n = \pm 1$, denoting the conduction and valence bands, respectively. According to the definition of Berry curvature, $\Omega(k) = \nabla \times \langle u(\mathbf{k})|i\mathbf{V}_i|u(\mathbf{k})\rangle$, where $u(k)$ is the periodic part of the Bloch wave function. We can obtain the Berry curvature associated with the valley,

$$\Omega_\eta^n(\mathbf{k}) = -\eta n \frac{a^2 t^2 \Delta_m}{2[(kat)^2 + (\Delta_m)^2]^{(3/2)}}.\qquad(5)$$

By tuning the band gap and the magnetovalley coupling strength, we obtained the Berry curvature for the three phases SOTI, QAVHI, and NI, respectively. They are shown in Figs. 4(a)–4(c), respectively, matching the results of the DFT calculations. It is worth noting that the valley polarization is reflected by the difference in Berry curvature. One of the distinguishable traits of the quantum anomalous valley Hall effect (QAVHI) is the evident shift from opposite polarities to consistent polarities in the Berry curvature of the K/K' valleys during a phase transition.

For characterizing the nature of the valleys matching the phase diagram, we can reveal it through the anomalous Nernst effect of thermal excitation. The valley-dependent anomalous

Nernst conductivities are defined as

$$\mathcal{N}_\eta = \frac{ek_B}{\hbar} \sum_n \int \frac{d^2k}{(2\pi)^2} \Omega_\eta^n \mathcal{S}_\eta^n(\mathbf{k}),\qquad(6)$$

where $\mathcal{S}_\eta^n$ is the entropy density, and f_k denotes the Fermi distribution function. At 300 K temperature, we can obtain the anomalous valley Nernst conductance (ANV) and the anomalous charge Nernst conductance (ANC):

$$\mathrm{ANV} = \mathcal{N}_k - \mathcal{N}_{k'}, \quad \mathrm{ANC} = \mathcal{N}_k + \mathcal{N}_{k'}.\qquad(7)$$

Figures 4(a)–4(c) show the anomalous Nernst conductivities for each of the three phases. In the context of QAVHI, the ANC intersects the zero-energy level just once, whereas for SOTI and NI, the ANC crosses the zero point three times. Therefore, the ANC does not perfectly distinguish between individual insulation phases. On the other hand, the ANVs of the three phases differ from each other. The ANV of QAVHI has three intersections with the Fermi energy level. The ANVs of SOTI and NI have only one intersection with the Fermi energy level, and they have opposite signs. Therefore, ANV is a perfect choice to distinguish the insulating phases. When the magnetic moment is perpendicular to the plane, the magnetovalley coupling strength reaches its maximum. By adjusting the gap size, a contour plot of the ANV with respect to the energy and gap is obtained, as shown in Fig. 4(d), and with this process accompanied by a fixed magnetic moment direction $\theta_z = 90°$. Figure 4(e) corresponds to a fixed energy level difference of $\Delta_e = -0.05$ eV, with magnetic moment
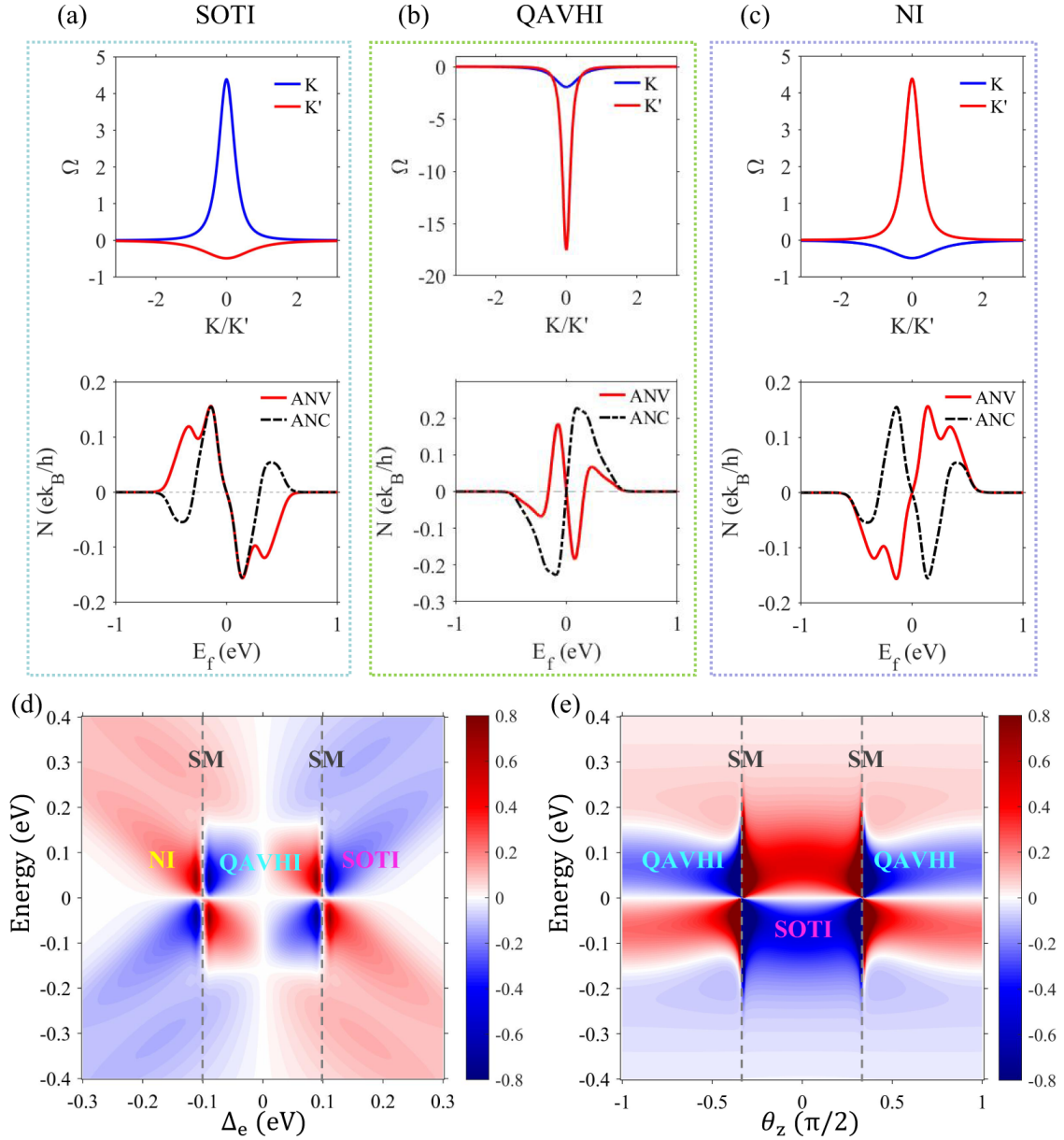
FIG. 4. (a)–(c) present the Berry curvature, ANC, and ANV of three insulation correlations: SOTI, QAVHI, and NI, respectively, concerning the K/K' valley. In (d), ANV is plotted as a function of energy and gap. Meanwhile, (e) illustrates the relationship between ANV, energy, and the direction of the magnetic moment θ_z. Phase boundaries are marked by gray dashed lines.

direction adjustment, resulting in a QAVHI-SOTI-QAVHI phase transition that perfectly matches the phase diagram.

IV. CONCLUSIONS

In summary, we employ the multiorbital tight-binding method to analyze the high-order topological properties of the 2D Janus ScClI. We give the complete phase diagram of ScClI's high-order topology, which is controlled by the magnetic moment direction θ_z and the orbital energy level interpolation Δ_e. The theoretically predicted phase transition process of SOTI-VHSM-QAVHI-VHSM-NI has been verified and realized from the DFT calculation results under strain engineering. Meanwhile, due to the valley polarization characteristics of the system, the three types of

insulators, SOTI, QAVHI, and NI, have different anomalous Nernst conductivities. By exploiting the anomalous Nernst effect, we construct an ANV map that corresponds to the topological phase diagram. Our findings can be extended to other similar types of two-dimensional materials, paving a way for future measurements and characterizations of higher-order topological phases in a broader range of materials.

ACKNOWLEDGMENTS

[1] M. Costa, B. Focassio, L. M. Canonico, T. P. Cysne, G. R. Schleder, R. B. Muniz, A. Fazzio, and T. G. Rappoport, Connecting higher-order topology with the orbital Hall effect in monolayers of transition metal dichalcogenides, Phys. Rev. Lett. **130**, 116204 (2023).

[2] S. Qian, G.-B. Liu, C.-C. Liu, and Y. Yao, C_n-symmetric higher-order topological crystalline insulators in atomically thin transition metal dichalcogenides, Phys. Rev. B **105**, 045417 (2022).

[3] J. Zeng, H. Liu, H. Jiang, Q.-F. Sun, and X. C. Xie, Multiorbital model reveals a second-order topological insulator in 1H transition metal dichalcogenides, Phys. Rev. B **104**, L161108 (2021).

[4] R. Li, N. Mao, X. Wu, B. Huang, Y. Dai, and C. Niu, Robust second-order topological insulators with giant valley polarization in two-dimensional honeycomb ferromagnets, Nano Lett. **23**, 91 (2023).

[5] J. Lee, J. Kwon, E. Lee, J. Park, S. Cha, K. Watanabe, T. Taniguchi, M.-H. Jo, and H. Choi, Spinful hinge states in the higher-order topological insulators WTe$_2$, Nat. Commun. **14**, 1801 (2023).

[6] Z. Guo, J. Deng, Y. Xie, and Z. Wang, Quadrupole topological insulators in Ta$_2$$M_3Te_5$ (M = Ni, Pd) monolayers, npj Quantum Mater. **7**, 87 (2022).

[7] F. Schindler, Z. Wang, M. G. Vergniory, A. M. Cook, A. Murani, S. Sengupta, A. Y. Kasumov, R. Deblock, S. Jeon, I. Drozdov *et al.*, Higher-order topology in bismuth, Nat. Phys. **14**, 918 (2018).

[8] R.-X. Zhang, F. Wu, and S. Das Sarma, Möbius insulator and higher-order topology in MnBi$_{2n}$Te$_{3n+1}$, Phys. Rev. Lett. **124**, 136407 (2020).

[9] Y. Xu, Z. Song, Z. Wang, H. Weng, and X. Dai, Higher-order topology of the axion insulator EuIn$_2$As$_2$, Phys. Rev. Lett. **122**, 256402 (2019).

[10] F. Schindler, A. M. Cook, M. G. Vergniory, Z. Wang, S. S. Parkin, B. A. Bernevig, and T. Neupert, Higher-order topological insulators, Sci. Adv. **4**, eaat0346 (2018).

[11] C. Chen, X.-T. Zeng, Z. Chen, Y. X. Zhao, X.-L. Sheng, and S. A. Yang, Second-order real nodal-line semimetal in three-dimensional graphdiyne, Phys. Rev. Lett. **128**, 026405 (2022).

[12] W. A. Benalcazar, B. A. Bernevig, and T. L. Hughes, Electric multipole moments, topological multipole moment pumping, and chiral hinge states in crystalline insulators, Phys. Rev. B **96**, 245115 (2017).

[13] W. A. Benalcazar, T. Li, and T. L. Hughes, Quantization of fractional corner charge in C_n-symmetric higher-order topological crystalline insulators, Phys. Rev. B **99**, 245151 (2019).

[14] W. A. Benalcazar, B. A. Bernevig, and T. L. Hughes, Quantized electric multipole insulators, Science **357**, 61 (2017).

[15] L. Cai, R. Li, X. Wu, B. Huang, Y. Dai, and C. Niu, Second-order topological insulators and tunable topological phase transitions in honeycomb ferromagnets, Phys. Rev. B **107**, 245116 (2023).

[16] N. Mao, R. Li, X. Zou, Y. Dai, B. Huang, and C. Niu, Ferroelectric higher-order topological insulator in two dimensions, Phys. Rev. B **107**, 045125 (2023).

[17] Y. Zhang, J. Tang, X. Dai, and Y. Xiang, Flexible dimensional hierarchy of higher-order topology in the stacked kagome-chain acoustic crystal, Commun. Phys. **6**, 130 (2023).

[18] H.-X. Wang, L. Liang, B. Jiang, J. Hu, X. Lu, and J.-H. Jiang, Higher-order topological phases in tunable C_3 symmetric photonic crystals, Photonics Res. **9**, 1854 (2021).

[19] M. Ezawa, Monolayer topological insulators: Silicene, germanene, and stanene, J. Phys. Soc. Jpn. **84**, 121003 (2015).

[20] K. Jana and B. Muralidharan, Robust all-electrical topological valley filtering using monolayer 2D-xenes, npj 2D Mater. Appl. **6**, 19 (2022).

[21] D. Xiao, G.-B. Liu, W. Feng, X. Xu, and W. Yao, Coupled spin and valley physics in monolayers of MoS$_2$ and other group-VI dichalcogenides, Phys. Rev. Lett. **108**, 196802 (2012).

[22] X. Zhou, R.-W. Zhang, Z. Zhang, W. Feng, Y. Mokrousov, and Y. Yao, Sign-reversible valley-dependent Berry phase effects in 2D valley-half-semiconductors, npj Comput. Mater. **7**, 160 (2021).

[23] J. Qi, X. Li, Q. Niu, and J. Feng, Giant and tunable valley degeneracy splitting in MoTe$_2$, Phys. Rev. B **92**, 121403(R) (2015).

[24] W.-Y. Tong, S.-J. Gong, X. Wan, and C.-G. Duan, Concepts of ferrovalley material and anomalous valley Hall effect, Nat. Commun. **7**, 13612 (2016).

[25] H. Tanaka, T. Higo, R. Uesugi, K. Yamagata, Y. Nakanishi, H. Machinaga, and S. Nakatsuji, Roll-to-roll printing of anomalous Nernst thermopile for direct sensing of perpendicular heat flux, Adv. Mater. **35**, 2303416 (2023).

[26] M. Li, H. Pi, Y. Zhao, T. Lin, Q. Zhang, X. Hu, C. Xiong, Z. Qiu, L. Wang, Y. Zhang *et al.*, Large anomalous Nernst effects at room temperature in Fe$_3$Pt thin films, Adv. Mater. **35**, 2301339 (2023).

[27] S. Roychowdhury, K. Samanta, P. Yanda, B. Malaman, M. Yao, W. Schnelle, E. Guilmeau, P. Constantinou, S. Chandra, H. Borrmann *et al.*, Interplay between magnetism and topology: Large topological Hall effect in an antiferromagnetic topological insulator, EuCuAs, J. Am. Chem. Soc. **145**, 12920 (2023).

[28] Y. Pan, C. Le, B. He, S. J. Watzman, M. Yao, J. Gooth, J. P. Heremans, Y. Sun, and C. Felser, Giant anomalous Nernst signal in the antiferromagnet YbMnBi$_2$, Nat. Mater. **21**, 203 (2022).

[29] Y. Li, J. Zhou, M. Li, L. Qiao, C. Jiang, Q. Chen, Y. Li, Q. Tao, and Z.-A. Xu, Enhanced anomalous Nernst effect by tuning the chemical potential in the topological kagome ferromagnet Fe$_3$Sn$_2$, Phys. Rev. Appl. **19**, 014026 (2023).

[30] H. Sawahata, N. Yamaguchi, S. Minami, and F. Ishii, First-principles calculation of anomalous Hall and Nernst conductivity by local Berry phase, Phys. Rev. B **107**, 024404 (2023).

[31] X.-Q. Yu, Z.-G. Zhu, G. Su, and A.-P. Jauho, Thermally driven pure spin and valley currents via the anomalous Nernst effect in monolayer group-VI dichalcogenides, Phys. Rev. Lett. **115**, 246601 (2015).

[32] G. Kresse and J. Furthmüller, Efficient iterative schemes for *ab initio* total-energy calculations using a plane-wave basis set, Phys. Rev. B **54**, 11169 (1996).

[33] G. Kresse and J. Furthmüller, Efficiency of *ab initio* total energy calculations for metals and semiconductors using a plane-wave basis set, Comput. Mater. Sci. **6**, 15 (1996).

[34] J. P. Perdew, K. Burke, and M. Ernzerhof, Generalized gradient approximation made simple, Phys. Rev. Lett. **77**, 3865 (1996).

[35] J. P. Perdew, K. Burke, and M. Ernzerhof, Perdew, Burke, and Ernzerhof reply, Phys. Rev. Lett. **80**, 891 (1998).

[36] K. Jia, X.-J. Dong, S.-S. Li, W.-X. Ji, and C.-W. Zhang, Spontaneous valley polarization and valley-nonequilibrium quantum anomalous Hall effect in Janus monolayer ScBrI, Nanoscale **15**, 8395 (2023).

[37] X.-S. Guo, S.-D. Guo, S.-N. Si, K. Cheng, K. Wang, and Y. S. Ang, Janus monolayer ScXY (X ≠ Y = Cl, Br and I) for piezoelectric and valleytronic application: a first-principle prediction, J. Phys.: Condens. Matter **35**, 405501 (2023).

[38] M. Iraola, J. L. Mañes, B. Bradlyn, M. K. Horton, T. Neupert, M. G. Vergniory, and S. S. Tsirkin, IrRep: Symmetry eigenvalues and irreducible representations of *ab initio* band structures, Comput. Phys. Commun. **272**, 108226 (2022).

[39] A. A. Mostofi, J. R. Yates, Y.-S. Lee, I. Souza, D. Vanderbilt, and N. Marzari, wannier90: A tool for obtaining maximally-localised Wannier functions, Comput. Phys. Commun. **178**, 685 (2008).

[40] Q. Wu, S. Zhang, H.-F. Song, M. Troyer, and A. A. Soluyanov, Wanniertools: An open-source software package for novel topological materials, Comput. Phys. Commun. **224**, 405 (2018).

[41] See Supplemental Material at http://link.aps.org/supplemental/10.1103/PhysRevB.109.035423 for (I) orbital verification of high-order topology, (II) robustness of high-order topology, (III) magnetic valley coupling effects and other DFT results, and (IV) valley-related anomalous Nernst conductivity and ANC map.